Renewable Energy 208 (2023) 465–480

Contents lists available at ScienceDirect

Renewable Energy

journal homepage: www.elsevier.com/locate/renene

Effect of a novel cooling window on a recuperated solar-dish Brayton cycle

J.H. de Beer [a], W.G. le Roux [a,*], A. Sciacovelli [b], J.P. Meyer [a,1]

[a] Department of Mechanical and Aeronautical Engineering, University of Pretoria, Private Bag X20, Hatfield, Pretoria, 0028, South Africa
[b] Birmingham Centre for Energy Storage (BCES), School of Chemical Engineering, University of Birmingham, UK

ARTICLE INFO

Keywords:
Turbocharger
Solar dish
Micro-turbine
Cooling window
Recuperator
Brayton cycle

ABSTRACT

A recuperated solar-dish Brayton cycle using an off-the-shelf turbocharger as a micro-turbine and a rectangular cavity receiver with integrated thermal storage is considered in this study. Due to the high temperatures that these solar receivers operate at, a considerable amount of heat is lost to the environment through the aperture, decreasing the solar-to-mechanical efficiency of the cycle. In this work, the heat losses from the solar receiver were reduced by utilising a novel glass channel on the inside of the cavity receiver, running parallel to the receiver walls and cooled by the working fluid (air) flowing from the compressor. The objective of this conceptual study was to investigate the impact of the novel air-cooled window on the performance of the cycle at steady state. An entropy generation minimisation technique combined with a SolTrace analysis was used. Results showed that the maximum solar-to-mechanical efficiencies were on average between 41% and 45% lower than for the cycle without the window. However, it was found that the exhaust temperature of the cycle with the window was higher. Therefore, a higher energy utilisation factor of between 9% and 11% was found when cogeneration was included.

1. Introduction

Since the development of the closed Brayton cycle in the 1930s, there have been many designs and experiments combining either an open or a closed Brayton cycle with a concentrated solar power system to generate electricity [1,2]. However, the very high operating temperatures of solar receivers used in concentrated solar power systems can significantly decrease the efficiency of such systems [3,4].

1.1. Background and previous work

A solar dish can be applied as the heat source for power generation using a Brayton cycle [5]. Air is an available and cost-effective working fluid for the Brayton cycle, and allows for the cycle to be hybridised using a combustion chamber. Much research has therefore been done on the optimisation and testing of solar receivers using air as working fluid, for operation in open Brayton cycles [6]. Bashir et al. [7] investigated the use of a metallic phase-change material (PCM) integrated into a solar receiver for short-term thermal energy storage in solar-dish gas turbine systems. Metallic phase-change materials can be used as thermal storage to provide a more stable turbine inlet temperature [8]. Thermal storage can therefore be implemented in a solar-dish Brayton cycle to balance out sudden fluctuations in solar radiation due to clouds [9].

Off-the-shelf turbochargers have been proposed to act as micro-turbines in solar-dish Brayton cycles, to reduce overall cycle costs [10,11]. In previous work, Le Roux and Sciacovelli [12] considered an open-cavity tubular solar receiver with integrated metallic PCM for short-term thermal storage, together with an off-the-shelf turbocharger for power generation in a recuperated solar-dish Brayton cycle. However, heat losses from the proposed open-cavity solar receiver negatively impacted the thermal efficiency of the solar receiver. Le Roux and Sciacovelli [12] found that the maximum total heat loss rate from the solar receiver was in the range of 12 kW when using a PCM at 1200 K and an inclination angle of 45°. Craig et al. [13] applied computational fluid dynamics (CFD) and ray tracing on an open-cavity tubular solar receiver similar to the one by Le Roux and Sciacovelli [12]. Craig et al. [13] found that the receiver had a total heat loss rate of 6.8 kW relative to a rated solar input power of 12.7 kW at a 0° inclination angle and an average receiver inner-surface temperature of 1053 K. Heat losses from the solar receiver can be decreased by decreasing the size of the aperture; however, this leads to the need for a more accurate and expensive

* Corresponding author. Department of Mechanical and Aeronautical Engineering, University of Pretoria, Private Bag X20, Hatfield, Pretoria, 0028, South Africa.
E-mail address: willem.leroux@up.ac.za (W.G. le Roux).
[1] Present address: Department of Mechanical and Mechatronic Engineering, Stellenbosch University; Private Bag X1, Matieland 7602, South Africa; Email: jpm2@sun.ac.za

https://doi.org/10.1016/j.renene.2023.02.085
Received 20 September 2022; Received in revised form 17 January 2023; Accepted 17 February 2023
Available online 21 February 2023

Nomenclature

A	Area, m^2
AR	Aspect ratio
a	Width of recuperator channel, m
b	Height of recuperator channel, m
BSR	Blade speed ratio
c	Linear fit constant
c_p	Constant pressure specific heat, J/kgK
D	Diameter, m
D_1	Difference 1, W
D_2	Difference 2, W
EUF	Energy utilisation factor
F	View factor
f	Friction factor
h	Heat transfer coefficient, W/m^2K
k	Thermal conductivity, W/mK
L	Length, m
L_s	Ensemble length, m
M	Mass, kg
m	Linear fit constant
$\dot{m}$	System mass flow rate, kg/s
N	Amount of glass divisions
N'	Speed of micro-turbine shaft, rpm
NTU	Number of transfer units
Nu	Nusselt number
n	Number of flow channels in one direction
P	Pressure, Pa
Pr	Prandtl number
$\dot{Q}$	Heat transfer rate, W
$\dot{Q}_{loss}$	Heat loss rate, W
$\dot{Q}_{net}$	Net heat transfer rate, W
$\dot{Q}^*$	Solar power available at the receiver cavity, W
R	Gas constant, J/kgK
Ra	Rayleigh number
Re	Reynolds number
r	Pressure ratio
$\dot{S}_{gen}$	Rate of entropy generation, W/K
s	Specific entropy, J/kgK
T	Temperature, K
T^*	Apparent temperature of the sun as an exergy source, K
t	Thickness, m
U	Overall heat transfer coefficient, W/m^2K
V	Velocity, m/s
v	Specific volume, m^3/kg
$\dot{W}$	Power, W
X_1	Additional net power output calculation 1, W
X_2	Additional net power output calculation 2, W
Z	Height, m

Greek Letters

α	Constant for heat transfer coefficient relation
β	Constant for heat transfer coefficient relation
Γ	Ratio between fluxes
Δ	Change in
ε	Emissivity
η	Efficiency
θ	Receiver inclination angle
λ	Focal length, m
ρ	Density, kg/m^3
σ	Stefan-Boltzmann constant, W/m^2K
ψ	Constant for heat transfer coefficient relation

Subscripts

0	Zero-pressure (for c_p)
1–11	Refer to Fig. 2 (for *T*, *P*, *V* and *Z*)
air	Air
abs	Absorbed
avg	Average
cold	Cold side
c	Compressor
chn	Channel
cav	Cavity
cond	Conduction
conv	Convection
f	Fluid
gl	Glass
hot	Hot side
hyd	Hydraulic
i	Index counter
init	Initial
in	At the inlet
ins	Insulation
int	Internal
j	Index counter
L	Based on the length
loss	Loss
max	Maximum
n	Glass section number
net	Net
opt	Optimum
outer	On the outside of the insulation
out	At the outlet
rad	Radiation
rec	Receiver
reg	Recuperator
s	Surface
sol	Solar
t	Turbine
tot	Total
w	To the water
win	Window
∞	Environment

solar dish. Some researchers have used glass covers in order to minimise heat losses from rectangular solar receivers [14–17]. However, keeping the glass covers cool under highly concentrated solar irradiation has proved to be a difficult task. A window cover on a solar receiver that is not cooled can crack or shatter due to the very high temperatures the glass is subjected to. This can lead to cost increases as well as pose safety hazards to the operators or maintenance personnel.

Solar receivers with window covers have been investigated in numerous literature studies. The glass must be able to withstand significant thermal loads from highly concentrated solar irradiation and reradiation from the inner-cavity walls. Thus, various strategies have been investigated to ensure the safety and durability of the glass cover solution. These strategies include manufacturing the glass with concave shapes to relieve thermal tension [18] or cooling the glass through forced convection with an appropriate heat transfer fluid [19]. A 250 kW_{th} tubular cavity receiver with a 3 mm thick, flat, uncoated quartz glass cover, which was investigated by Too et al. [20], showed that an increase of nearly 17% in the receiver's thermal efficiency was possible.

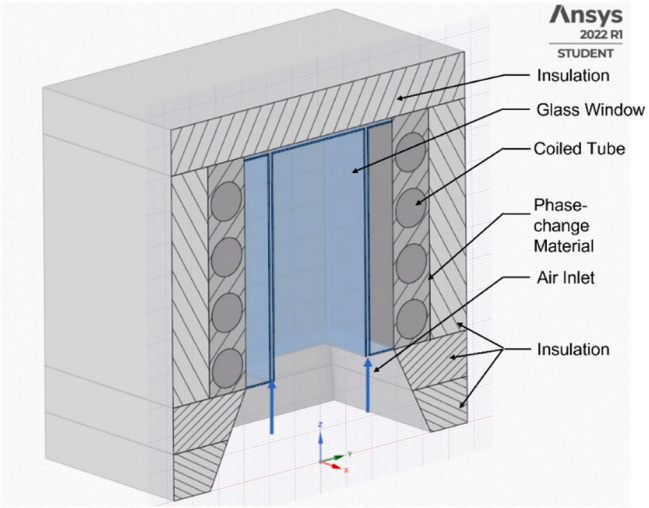

Fig. 1. 3D section view (representation) of the receiver with the cooling window concept.

In a CFD study by Cui et al. [14], a 5 mm-thick quartz cover with a selective coating was used. The simulations showed that the heat losses were reduced by 36% compared with those of the uncovered receiver.

Li et al. [3] investigated a double-window cover concept in which the aperture of the receiver was covered with a glass pane and the second glass pane was placed a certain distance into the receiver cavity. Li et al. [3] found that the total efficiency increased as the cavity size, inner-window thickness, emissivity of the inner walls, and distance between the two windows increased. The peak temperature of the outer window was about 39 K–83 K lower than for a configuration with only one window cover [3]. Uhlig and Röger [18] combined the idea of using a concave shape to relieve thermal stresses and forced convection to cool the glass. The receiver consisted of a concave quartz inner-window cover, which was cooled by air bled from the compressor to ensure the cooling air had the same pressure before entering the receiver [18]. The outlet gap geometry and inlet temperature were altered to find the most efficient cooling, the lowest pressure drop and lowest mass flow rate. The design was tested experimentally and compared with numerical simulations with acceptable accuracy.

Wang et al. [19] investigated a volumetric solar receiver with glass cover cooling. The cooling air was pumped from a compressor and fed back into the cycle after passing over the glass cover. The cooling window was placed perpendicular to the receiver walls and parallel to the aperture. The investigation was conducted numerically (with the finite volume method) and experimentally (with three all-day tests). An outlet air temperature of 1003 K and a thermal efficiency of 63.1% were observed [19].

1.2. Novelty and contribution of this work

In this work, a novel air-cooled glass window is proposed for the open-cavity tubular solar receiver that was investigated by Le Roux and Sciacovelli [12]. The novel air-cooled glass window is placed on the inside of the solar receiver cavity, parallel to the receiver walls and perpendicular to the aperture (different from the air-cooled glass windows that were mentioned above). Furthermore, the novel cooling window is integrated with a recuperated solar-dish Brayton cycle, by using air directly from the compressor to cool the window. This work also considers off-the-shelf turbochargers for the micro-turbine and an open-cavity tubular receiver with integrated PCM as thermal storage, as was done by Le Roux and Sciacovelli [12]. The study analyses the impact of the novel air-cooled window on the solar-to-mechanical conversion

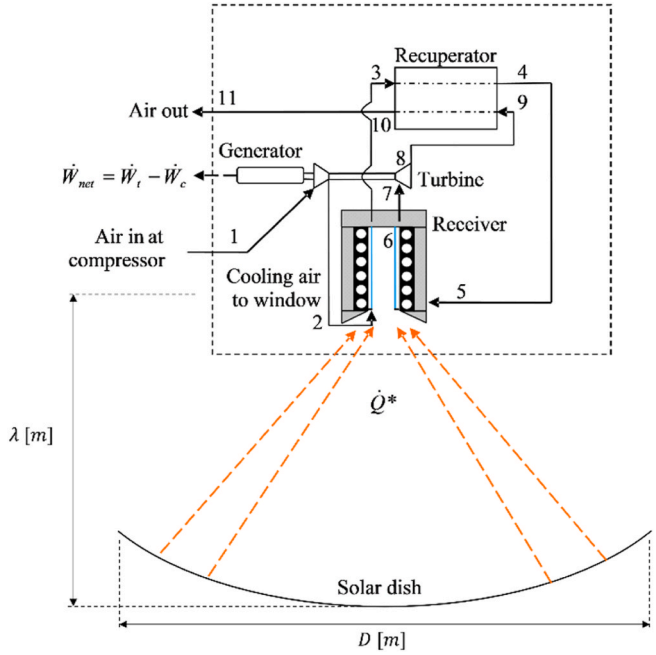

Fig. 2. Recuperated solar-dish Brayton cycle with receiver window cooling, adapted from Le Roux and Sciacovelli [12].

efficiency, net power output, energy utilisation factor (when including cogeneration), required solar input power, and consequently, the required dish size for steady-state operation at a certain phase-change temperature.

2. System description

A glass window is proposed on the inside of the receiver cavity, parallel to the rectangular receiver walls. This concept consists of two glass panes forming a channel in which cooling air flows (see Fig. 1 for a 3D visualisation of the concept created with *ANSYS*). There are four channels, one on each side of the receiver, as well as a channel parallel to the top wall of the receiver. The glass is cooled by air coming directly from the compressor. The stainless-steel solar receiver cavity has a total height of 0.5 m and an aperture area of 0.25 m × 0.25 m (identical to Le Roux and Sciacovelli [12]). Fig. 2 shows the recuperated solar-dish Brayton cycle with short-term thermal storage as well as the position of the novel cooling window (in blue). The cycle uses air as working fluid in an open-cycle configuration. Air enters the radial compressor (Position 1 in Fig. 2), which is driven by the turbine. The turbine also acts as a generator to provide shaft power to an electrical load [10]. The concentrated solar power (orange arrows) heats the inner-cavity walls of the solar receiver, which contains the phase-change thermal storage material. The thermal storage material heats the air flowing through a stainless steel coil [12]. The recuperator allows for increased cycle efficiencies and operation at lower pressure ratios [21,22]. The hot exhaust air can be used for cogeneration (see, for example, Ref. [23]).

3. Methodology

This section presents the most important assumptions that were made in the analysis. The modelling of the solar receiver with the integrated glass window and cooling is described with the first law of thermodynamics. Gaussian elimination was used to calculate the glass surface temperature and the amount of heat the glass transfers to the cooling air. The complete cycle modelling used an entropy generation minimisation technique to optimise the maximum cycle net power

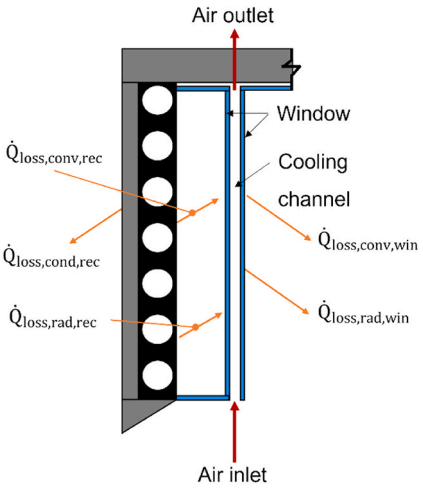

Fig. 3. 2D section view of the receiver (representation) with heat losses.

output with a recuperator and micro-turbine. The models were set up to predict the solar-to-mechanical efficiency of the cycle, the net power output of the cycle, the required solar input power, and the glass surface temperature. The recuperator geometry, receiver phase-change temperature and turbine pressure ratio were variables in this study. Performance maps were created, which could be used for further analyses where cost, net power output, turbine pressure ratio and phase-change temperature were considered.

3.1. Assumptions

It was assumed that the phase-change material, as well as the stainless-steel inner-cavity walls and tube surface, were at a constant temperature (the melting temperature of the PCM). The mass flow rate from the compressor was divided equally between the five window channels (one on each side of the receiver, as well as one at the top) and each glass window was 3 mm thick. The width between two glass windows forming a channel was initially arbitrarily chosen as 6.8 mm and the simulations were carried out with this channel width; however, the channel width was also later investigated as a parameter. Conduction heat losses from the cooling window were not considered in this study and were expected to be negligible.

3.2. Receiver and glass modelling

The receiver and the glass window were modelled using the first law of thermodynamics. Fig. 3 shows the heat losses from the window to the environment through the receiver aperture as well as the heat gain on the window from the inner-receiver wall. From an energy balance at steady state, the net heat transfer rate at the glass window is given by:

$$\dot{Q}_{net,win} = \dot{Q}^{*}_{win} + \dot{Q}_{abs} - \dot{Q}_{loss,rad,win} - \dot{Q}_{loss,conv,win} \tag{1}$$

where $\dot{Q}_{abs} = \dot{Q}_{loss,rad,rec} + \dot{Q}_{loss,conv,rec}$, which represents the heat gain on the window from the inner-receiver wall (see Fig. 3), while $\dot{Q}^{*}_{win}$ represents the absorbed solar heat as found from SolTrace (see the following subsection for a description of the SolTrace analysis).

3.2.1. SolTrace model

SolTrace can model concentrated solar power (CSP) systems using Monte Carlo ray-tracing methodologies [24]. In this work, the solar receiver geometries were fixed while the dish size was allowed to vary using a fixed rim angle of 45°. The SolTrace script was therefore written in such a way that when the dish size was changed, the receiver position relative to the solar dish would be adjusted accordingly to have the parabolic dish's focal point on the receiver with minimal spillage.

The solar dish accuracy, optical properties and dish size are important factors that can significantly impact the total cost and cycle efficiency. The dish surface was modelled as having a reflectivity of 85% and both a specularity and slope error of 2 mrad. A solar irradiance of 1000 W/m^2 was assumed. The receiver cavity walls were modelled as oxidised stainless steel with an assumed reflectance of 15% [10]. The glass had an assumed reflectivity of 8%, transmissivity of 86% and absorptivity of 6% for solar radiation per window [25]. A pillbox sunshape was assumed with the parameter for the pillbox chosen as the half-angle width of 4.65 mrad. Each of the glass panes was modelled with a refraction index of 1.5, with an air entity on each side with a refraction index of 1. This was done to capture the refraction of light as it travelled through the glass, as recommended by Wendelin et al. [24]. Since SolTrace uses ray tracing to compute heat flux, more sun rays mean increased accuracy of the solutions and therefore, 1 million sunrays were used with a seed value of '123' throughout the simulations.

3.2.2. Radiation heat loss model

The emissivity of the inner-cavity wall was assumed to be 0.7 for oxidised stainless steel at 1000 K [12]. The radiation heat loss rate from a surface can typically be calculated with Eq. (2) [25]:

$$\dot{Q}_{loss,rad} = \varepsilon\sigma A\left(T_s^4 - T_\infty^4\right) \tag{2}$$

When calculating the surface temperature of the glass, the view factor (sometimes called the shape factor) is a very important aspect to consider. The view factor determines how much a certain part of the glass is exposed to the aperture (environment), inner-cavity wall, or the other glass panes. The radiation heat transfer rate in different sections of the inner-receiver wall was calculated using Eq. (3) [10]:

$$\dot{Q}_{loss,rad,n} = A_n \sum_{j=1}^{N} F_{n\to j}\left(\varepsilon_n\sigma T_{s,n}^4 - \varepsilon_j\sigma T_{s,j}^4\right) \tag{3}$$

Eq. (3) was also used to determine the radiation heat loss rate from the glass to the aperture. The emissivity of the glass was assumed to be constant at 0.88 [17]. The radiation heat transfer from a hot surface to a cooler surface is proportional to the fourth power of the surface temperatures of the two surfaces. To be able to use Gaussian elimination, the fourth-power temperature terms were assumed to have a linear form, $m_1 T_{s,n} + c_1$, according to Ref. [10]. For radiation heat loss from the glass between 500 K and 800 K, a linear regression line with a coefficient of determination of 0.96 was used.

Since there were two glass panes per channel, the effective transmissivity for infrared radiation from the inner-cavity walls became almost negligible. Therefore, in this work, it was assumed that for infrared radiation, the reflectivity and absorptivity of the double-glass window were 90% and 10% respectively.

3.2.3. Convection heat loss model

Convection heat transfer will occur on the inside of the cavity, on the inside of the cooling channel, on the inside of the air gap between the window and the cavity wall, and on the inside of the coiled tube in the receiver. As in the work of Le Roux and Sciacovelli [12], the Dittus-Boelter equation was used to model internal forced convection on the inside of the coiled tube. Forced internal convection also occurred on the inside of the cooling channels formed by two glass panes (see Fig. 3). Since the glass channels were rectangular, the Reynolds number had to be altered by using the hydraulic diameter, which is given by Eq. (4) [25]:

$$D_{hyd} = \frac{2ab}{a+b} \tag{4}$$

For laminar flow, the Nusselt numbers and friction factors for the

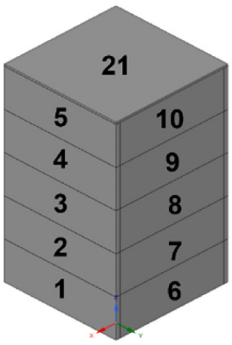

Fig. 4. Numbering system used for glass sections.

glass channels (noncircular tubes) are found in Ref. [25] assuming constant heat flux. The heat transfer coefficient was calculated by rearranging Eq. (5):

$$Nu = \frac{hD_{hyd}}{k} \tag{5}$$

For turbulent flow (assuming the Reynolds number is greater than 4000), the Nusselt number for the glass channels was calculated using the following equation [26]:

$$Nu = \frac{(f/8)(Re - 1000)Pr}{1 + 12.7\left(\frac{f}{8}\right)^{0.5}\left(Pr^{\frac{2}{3}} - 1\right)} \tag{6}$$

The friction factor, f, in Eq. (6) was found using the Petukhov equation [27] for turbulent flow in smooth tubes, as shown in Eq. (7):

$$f = (0.790\ ln(Re) - 1.64)^{-2} \tag{7}$$

It must be noted that there were different Nusselt number correlations, and thus different heat transfer coefficients, for the different flow regimes. The code that calculated the heat transfer coefficient used an if-statement to determine the appropriate Nusselt number based on the Reynolds number.

Natural convection on the inside of the cavity is a relatively complex phenomenon. Paitoonsurikarn and Lovegrove [28] showed that a parameter described as the ensemble cavity length scale, L_s, could be used to account for the effects of cavity geometric parameters and inclination [29,30]. The proposed ensemble length, L_s, is given by Eq. (8):

$$L_s = \left| \sum_{i=1}^{3} \alpha_i\ cos(\theta + \psi_i)^{\beta_i} L_i \right| \tag{8}$$

Eq. (8) depends on the cavity dimensions as well as the inclination angle of the receiver. The index, i, in Eq. (8) depends on three length scales of the receiver, namely the cavity width, depth and aperture size, represented by the symbol, L_i. The constants α_i, β_i and ψ_i from Eq. (8) are summarised in Paitoonsurikarn and Lovegrove [28]. The Nusselt correlation has the following form [28]:

$$Nu_L = 0.0196\ Ra_L^{0.41}\ Pr^{0.13} \tag{9}$$

The Rayleigh and Prandtl numbers in Eq. (9) were evaluated at the film temperature, which is the average between the glass surface temperature, T_s, and the ambient temperature, T_∞. The heat transfer coefficient on the inside of the cavity was then calculated by rearranging Eq. (10):

$$Nu = \frac{h_{cav}L_s}{k} \tag{10}$$

The heat loss due to convection per window section was calculated with the average heat transfer coefficient for the whole cavity and is given by Eq. (11):

$$\dot{Q}_{loss,conv} = h_{cav}A_{gl}(T_s - T_\infty) \tag{11}$$

Lastly, the convection heat transfer in the enclosure (between each inner-cavity wall and glass pane, see Fig. 3) depends on the aspect ratio and Rayleigh number of the enclosure. In CFD simulations by Pendyala et al. [31], the authors developed Nusselt number correlations applicable to air as a working fluid:

$$Nu = 1.46 \times 10^{-5}(AR)^{0.19}(ln(Ra))^{3.228} \tag{12}$$

Eqs. (10) and (12) were used to find the heat transfer coefficient in the enclosure. The convection heat loss from the window is included in Eq. (1).

3.2.4. Pressure drop

For fully developed flow in a circular duct, the pressure drop is given by Eq. (13) [25]. For a rectangular duct, the hydraulic diameter, D_{hyd}, was used instead, as calculated by Eq. (4).

$$\Delta P = f\frac{L}{D}\frac{\rho V_{avg}^2}{2} \tag{13}$$

The symbols a and b in Eq. (4) refer to the channel width and height respectively. For laminar flow in a duct with constant heat flux, the friction factor can be interpolated from Çengel & Ghajar [25] at the specific aspect ratio, a/b. For turbulent flow, Eq. (7) can be used to calculate the friction factor in the rectangular duct. Note that the pressure drop in the solar receiver coil was determined according to Le Roux & Sciacovelli [12].

3.2.5. Numerical methods

The temperature profile of the glass was determined by dividing each of the four glass panes into several equally sized sections (see Fig. 4). Each of the four sides of the rectangular receiver was divided into five sections, which gave each section a height of 0.1 m. The top section was also covered with glass in the simulation to account for the view factor to the top. The top glass pane was not divided into sections to limit computational time.

Fig. 4 shows the numbering system used for the glass sections, where the top section was added to the end of the numbering system. The proposed method was based on the method put forward by Ref. [10]. The main difference was that the flow was not modelled to flow in a coil but rather from the bottom to the top of the window.

In this conceptual study, the temperature profile and the net heat transfer rate at the various sections of each glass window were found with Eq. (14) [10]. It was therefore assumed that each glass channel section had a constant temperature on both sides of the channel. Note that the mass flow rate, $\dot{m}_{chn}$, used in all the equations that involved the windows was equal to the mass flow rate at Point 1 in Fig. 2 divided by five.

$$\dot{Q}_{net,n,win} = \frac{\left(T_{s,n} - \sum_{i=1}^{n-1}\left(\frac{\dot{Q}_{net,i}}{\dot{m}_{chn}c_{p0}}\right) - T_{in,init}\right)}{\left(\frac{1}{h_{chn}A_n} + \frac{1}{2\dot{m}_{chn}c_{p0}}\right)} \tag{14}$$

Eq. (14) was derived from the definition of fluid temperature at the centre of a control volume as well as the definition of convection heat transfer, according to Eq. (15) and Eq. (16) respectively [10].

$$T_{f,n} = T_{in,n} + \frac{T_{out,n} - T_{in,n}}{2} = T_{in,n} + \frac{\dot{Q}_{net,n,win}}{2\dot{m}_{chn}c_{p0}} \tag{15}$$

$$\dot{Q}_{net,n,win} = h_{chn}A_n\left(T_{s,n} - T_{f,n}\right) \tag{16}$$

Eq. (14) used the outlet temperature of the compressor as $T_{in,init}$. The outlet air temperature from each section, $T_{out,n}$, was calculated from the heat gained at the previous glass sections. Eq. (6) was used to calculate the heat transfer coefficient in Eq. (14). By using Eq. (3) and Eq. (11) and

substituting into Eq. (1), Eq. (17) could be found, which was written in terms of the unknown net heat transfer rates and surface temperatures of each glass section according to the numbering in Fig. 4. Note that for the radiation heat loss term, the radiation heat transfer from one glass side to another and the radiation heat loss to the aperture were included. This equation could be simplified further by using the linear approximation (as discussed in Section 3.2.2).

$$\dot{Q}_{net,n,win} = \dot{Q}^{*}_{n,win} + \dot{Q}_{abs,n} \quad -A_n\varepsilon\sigma\left(m_1 T_{s,n} + c_1\right) + A_n\varepsilon\sigma\sum_{j=1}^{N} F_{n\to j}\left(m_1 T_{s,j} + c_1\right) + A_n\varepsilon_\infty\sigma F_{n\to\infty} T_\infty^4 - h_{n,cav}A_n\left(T_{s,n} - T_\infty\right) \tag{17}$$

The $\dot{Q}_{abs,n}$ term in Eq. (17) is the radiation and convection heat transfer that was transferred from the inner-receiver wall to the window. Eq. (5) was used to calculate the heat transfer coefficient in Eq. (17). By using Gaussian elimination in *Octave*, the surface temperatures ($T_{s,n}$) and net heat transfer rates ($\dot{Q}_{net,n,win}$) of the window could be calculated by solving Eq. (14) and Eq. (17) simultaneously. The outlet air temperature of the cooling window was also of importance because the outlet air was directly fed back into the Brayton cycle (Position 3 in Fig. 2). The outlet air temperature was calculated by rearranging Eq. (18) (energy balance) and solving for $T_{air,out}$.

$$\dot{Q}_{net,win} = \dot{m}_{chn}c_{p0}\left(T_{air,out} - T_{air,in}\right) \tag{18}$$

The mass flow rate in Eq. (18) was one fifth of the full mass flow rate calculated from the corrected mass flow rate of each turbocharger at steady state (see Section 3.3.3). Eq. (18) could also be used to check whether the Gaussian elimination function had been solved correctly because $\dot{Q}_{net,win}$ had to be equal to the sum of the heat transfer rates that were calculated at each section of the window using Eq. (16). The outlet air temperature was used in modelling the complete cycle in the following sections.

3.3. Complete cycle modelling

The receiver phase-change temperature, chosen turbocharger, turbine operating point, and cooling channel width were parameters in the study. The complete cycle was modelled in the same manner as in the study by Le Roux and Sciacovelli [12]. The existing code by Le Roux and Sciacovelli [12] was modified to account for the heat gain of the air in the cooling window by including the methodology that was presented in Section 3.2. The variables were the recuperator channel width, height, length and number of parallel flow channels. The dimensions of the open-cavity tubular solar receiver stayed constant in the analysis and were the same as those used in the study by Le Roux and Sciacovelli [12].

3.3.1. Solar receiver

The aperture area of the receiver was fixed at 0.25 m × 0.25 m, the tube's inner diameter was 0.0833 m, and the tube length was 8 m [12]. The solar rays were concentrated by the solar dish and were absorbed by the receiver's inner-cavity wall after being transmitted through the glass window. The metallic phase-change material absorbed the heat from the concentrated solar radiation and stored it, but also transferred it to the heat transfer fluid (HTF), which flowed on the inside of the coiled tube. The coiled tube receiver was modelled as a constant surface temperature tube, with the assumption that the tube surface temperature, $T_{s,rec}$, was equal to the PCM melting temperature [12]. For steady-state operation, the exit temperature of the receiver air was calculated with Eq. (19) and the net heat transfer rate with Eq. (20) [25].

$$T_{out} = T_{s,rec} - \left(T_{s,rec} - T_{in}\right)e^{-\frac{h_{rec}A_s}{\dot{m}c_{p0}}} \tag{19}$$

$$\dot{Q}_{net,rec} = h_{rec}A_s\frac{\left(T_{in} - T_{out}\right)}{ln\left[\frac{T_{s,rec} - T_{out}}{T_{s,rec} - T_{in}}\right]} \tag{20}$$

It should be noted that the heat transfer coefficient, h_{rec}, in Eq. (20) is for the inside of the coiled tube and was calculated according to Le Roux & Sciacovelli [12]. The required solar power at the cavity walls was found using Eq. (21) [12].

$$\dot{Q}^{*}_{rec} = \dot{Q}_{loss,cond,rec} + \dot{Q}_{loss,conv,rec} + \dot{Q}_{loss,rad,rec} + \dot{Q}_{net,rec} \tag{21}$$

The heat losses due to conduction from the receiver to the environment were calculated according to Ref. [10]:

$$\dot{Q}_{loss,cond,rec} = \frac{A\left(T_{s,rec} - T_\infty\right)}{1.86} \tag{22}$$

where it was found that $\left(1/h_{outer} + t_{ins}/k_{ins}\right) \approx 1.86$ for receiver aperture sizes of up to 2 m [10]). The convection heat loss from the receiver to the window through the air gap between the windows was calculated with Eq. (11), where the heat transfer coefficient was calculated with Eq. (5) and the heat transfer was from the hot inner-cavity wall to the window. The radiation heat loss was calculated with a modified form of Eq. (2). Instead of having radiation heat loss to the environment, the radiation heat loss was from the inner-cavity wall to the glass, thus T_∞ in Eq. (2) was replaced by $T_{s,win}$.

The cycle optimisation code used a while loop to iterate the code and within the loop, Eq. (20) was used to calculate $\dot{Q}_{net,rec}$. The SolTrace model was run with five different solar dish sizes, namely dish diameters of 4.8, 6, 7.2, 8.4 and 9.6 m. Since the focal length of the solar dish is dependent on the size of the dish, the calculation of the focal length was coded into the SolTrace model to update the model as the dish size updated. The rim angle of the dish was kept constant at 45°. From the SolTrace analysis, a relationship was found between the solar flux on the glass panes and the inner-receiver walls, i.e., the relationship between $\dot{Q}^{*}_{win}$ and $\dot{Q}^{*}_{rec}$. The relationship was found to have the form of

$$\dot{Q}^{*}_{win} = m\dot{Q}^{*}_{rec} + c \tag{23}$$

and a function was written that outputs the function parameters m and c. It is important to note that $\dot{Q}^{*}_{win}$ only included the solar heat flux contribution and not the reradiation from the inner-cavity wall. The total required solar power was used further in the analysis and was given by Eq. (24), which is a function of the dish size and can be used to estimate the dish size required for steady-state cycle operation.

$$\dot{Q}^{*}_{tot} = \dot{Q}^{*}_{win} + \dot{Q}^{*}_{rec} \tag{24}$$

However, the code that calculated the temperature profile of the window required the solar flux on the window to be a distribution (per window section) instead of a total to function correctly. From the five SolTrace cases, the ratio of the solar flux distribution on each glass division could be determined. This ratio was calculated as follows:

$$\Gamma = \frac{Heat\ flux\ per\ division}{Total\ heat\ flux\ per\ side} \tag{25}$$

A function was made that interpolated between the five different dish size heat flux ratios. This distribution was used as an input to the code. The code calculated the glass surface temperature, which was used to calculate the heat losses from the window by using Eq. (3) and Eq. (11). Eq. (21) was then used to find $\dot{Q}^{*}_{rec}$, which was used in Eq. (23). The solar heat flux, $\dot{Q}^{*}_{win}$, was used in Eq. (1) to find the net heat transfer rate on the window, $\dot{Q}_{net,win}$. The neat heat transfer rate was used to find the change in temperature between Positions 2 and 3 (in Fig. 2) in the cycle with:

Table 1
Recuperator variables.

Variable	Range
Width of recuperator channel, a (mm)	150-450 (step size: 75)
Recuperator channel height, b (mm)	1.5–4.5 (step size: 0.75)
Length of recuperator, L_{reg} (m)	0.5–3.5 (step size: 0.75)
Recuperator number of parallel flow channels, n	15-45 (step size: 7.5)

$$\Delta T_{2-3} = \frac{\dot{Q}_{net,win}}{\dot{m}c_p} \tag{26}$$

The temperature change (Eq. (26)) was then used to calculate the temperature at Position 3 in Fig. 2 as follows:

$$T_3 = T_2 + \Delta T_{2-3} \tag{27}$$

which was iterated each time the while loop was executed.

3.3.2. Recuperator

The same plate-type counterflow recuperator model was considered in this study as the one used by Le Roux and Sciacovelli [12] (with channel width a, channel height b, channel length, L_{reg}, and number of flow channels in one direction, n). The pressure drop through the recuperator with rectangular channels was calculated according to Section 3.2.4 using the hydraulic diameter. The forced convection heat transfer coefficients for the hot and cold sides of the channel (h_{hot} and h_{cold}) were calculated to be able to calculate the overall heat transfer coefficient, U. The overall heat transfer coefficient, therefore, depended on the Reynolds numbers, aspect ratios and average temperatures. The effectiveness of the recuperator was found by using a modified effectiveness-*NTU* method that includes heat loss to the environment [12].

3.3.3. Power output

Octave was used to implement an entropy generation minimisation technique to calculate the maximum solar-to-mechanical efficiency, the net power output and the required solar input power for receiver phase-change temperatures ranging from 900 K to 1200 K while considering three different off-the-shelf turbochargers and several different recuperator geometries (see Table 1 and Le Roux and Sciacovelli [12]). The range of the recuperator length was changed to 0.5–3.5 m instead of the 1.5–3.5 m used in Le Roux and Sciacovelli [12]. A smaller recuperator length was expected because the air entering the recuperator at State 3 should already have gained significant heat from the window, and the recuperator thus needed to exchange less heat to get the receiver's inlet air to the same temperature.

The turbine pressure ratio (r_t) was used as a parameter in the analysis, as was done in the work by Le Roux and Sciacovelli [12]. The turbine map provides the corrected turbine mass flow rate in terms of the turbine pressure ratio. The actual mass flow rate, blade speed ratio (*BSR*) and turbine efficiency were calculated as shown in Le Roux and Sciacovelli [12] using an interpolation routine involving the shaft speed.

Three commercial turbochargers were considered in this analysis: the *GT1241*, *GT2052* and *GT2860RS* from *Garrett Motion* in the USA. The *Octave* program had the same structure as described in Le Roux and Sciacovelli [12]; however, the solar receiver part of the code was changed to include the cooling window. The program had the following structure:

For the three different turbochargers,

for $T_s = 900$ K–1200 K at step size of 100 K,
for each turbine pressure ratio (r_t) in the operating range of the turbine,
for each recuperator geometry combination (625 different combinations of a, b, L_{reg} and n),

- Find the net power output and the solar-to-mechanical efficiency of the cycle.
- Find required solar input power for steady-state operation at the phase-change temperature.

It was assumed that the heat losses in the pipes connecting each of the components were negligible. To find the temperatures and pressures in the cycle, an iteration routine was used along with the recuperator effectiveness and the compressor and turbine isentropic efficiencies. Note that $P_1 = P_{10}$ (see Fig. 2). By doing an exergy analysis for the recuperated solar-dish Brayton cycle and assuming $V_1 = V_{11}$ and $Z_1 = Z_{11}$, the net output power equation can be shown in Eq. (28) [32]. Eq. (29) shows the total entropy generation rate as a function of the pressures and temperatures of the cycle (see Fig. 2).

$$\dot{W}_{net} = -T_\infty \dot{S}_{gen,int} + \left(1 - \frac{T_\infty}{T^*}\right)\dot{Q}^* + \dot{m}c_{p0}(T_1 - T_{11}) - \dot{m}c_{p0}\, ln\left(\frac{T_1}{T_{11}}\right) \tag{28}$$

$$\begin{aligned}\dot{S}_{gen,int} = &\left[-\dot{m}c_{p0}\, ln\left(\frac{T_1}{T_2}\right) + \dot{m}Rln\left(\frac{P_1}{P_2}\right)\right]_{compressor} \\ &+ \left[\dot{m}c_{p0}\, ln\left[\frac{T_{10}T_4}{T_9T_3}\left(\frac{P_{10}P_4}{P_9P_3}\right)^{-\frac{R}{c_{p0}}}\right] + \frac{\dot{Q}_{loss,reg}}{T_\infty}\right]_{recuperator} \\ &+ \left[-\frac{\dot{Q}^*_{rec}}{T^*} + \frac{\dot{Q}_{loss,cond,rec}}{T_\infty} + \dot{m}c_{p0}\, ln\left(\frac{T_6}{T_5}\right) - \dot{m}R\, ln\left(\frac{P_6}{P_5}\right)\right]_{receiver} \\ &+ \left[-\dot{m}c_{p0}\, ln\left(\frac{T_7}{T_8}\right) + \dot{m}R\, ln\left(\frac{P_7}{P_8}\right)\right]_{turbine} \\ &+ \left[-\dot{m}c_{p0}\, ln\left(\frac{T_2}{T_3}\right) + \dot{m}Rln\left(\frac{P_2}{P_3}\right) + \frac{\dot{Q}_{loss,win}}{T_\infty} - \frac{\dot{Q}^*_{win}}{T^*}\right]_{window}\end{aligned} \tag{29}$$

Note that Eq. (29) indicates that the radiation and convection heat losses from the receiver's inner wall were absorbed by the window and the terms cancelled out in the entropy generation rate equations with only the conduction heat loss from the receiver still being present. The solar-to-mechanical efficiency was calculated with Eq. (30), where $\dot{Q}^*_{tot}$ included the solar heat gain of the receiver and the window.

$$\eta_{sol} = \frac{\dot{W}_{net}}{\dot{Q}^*_{tot}} \tag{30}$$

3.3.4. Energy utilisation factor

Another important cycle performance metric to consider was the energy utilisation factor (*EUF*), which indicated the extent to which the cycle could convert the available solar power into useable power and heat [33]. The *EUF* was calculated by using Eq. (31) [33] and assuming a water heat exchanger effectiveness, η, of 65%:

$$EUF = \frac{\left(\dot{W}_{net} + \eta\dot{Q}_{max,T_{11-1}}\right)}{\dot{Q}^*_{tot}} \tag{31}$$

where the quantity $\dot{Q}_{max,T_{11-1}}$ is the maximum potential for heat generation relative to the environment:

$$\dot{Q}_{max\ ,T_{11-1}} = \dot{m}c_{p0}(T_{11} - T_1) \tag{32}$$

The temperature of the environment, T_1, was taken to be 300 K and the cycle's exhaust temperature, T_{11}, was calculated with the numerical analysis described in this section. The constant pressure specific heat, c_{p0}, was calculated at the average temperature between T_1 and T_{11}.

4. Results

This section presents the results of the numerical analysis with a focus on the impact of the air-cooled window on the performance of the system. The results of the required solar input power, net power output

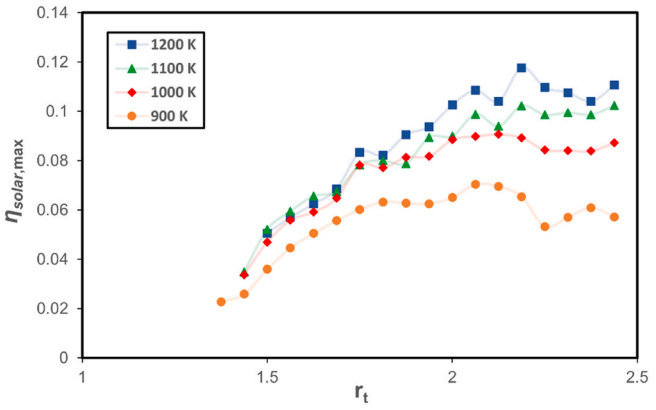

Fig. 5. Maximum solar-to-mechanical efficiency of the cycle for different turbine pressure ratios and receiver phase-change temperatures from 900 K to 1200 K (for *GT1241*).

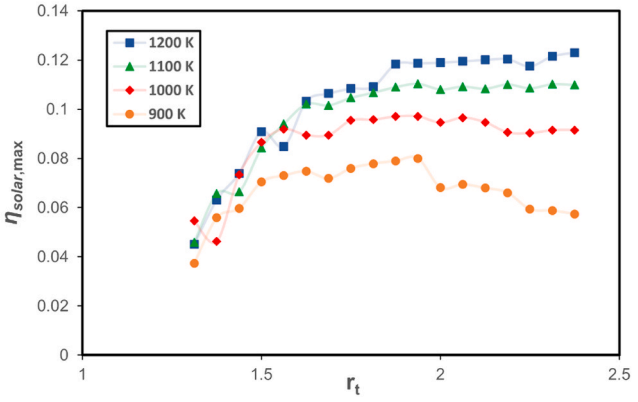

Fig. 6. Maximum solar-to-mechanical efficiency of the cycle for different turbine pressure ratios and receiver phase-change temperatures from 900 K to 1200 K (for *GT2052*).

and cycle temperatures at maximum solar-to-mechanical efficiency are presented. The impact of different cooling window channel widths on the pressure drop, heat transfer, temperature change and glass surface temperature is also presented. Finally, the impact of the novel cooling window on the performance of the cycle is discussed.

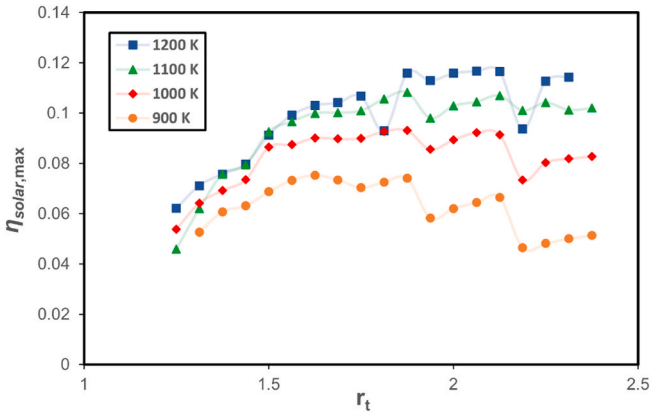

Fig. 7. Maximum solar-to-mechanical efficiency of the cycle for different turbine pressure ratios and receiver phase-change temperatures from 900 K to 1200 K (for *GT2860RS*).

4.1. Maximum solar-to-mechanical efficiency

The results in this section were produced with a cooling channel width of 6.8 mm. This specific channel width was chosen based on initial pressure drop calculations to keep the pressure drop below 1 kPa. The code was used to iterate through all the turbochargers' different pressure ratios as well as the different recuperator geometries. The maximum solar-to-mechanical efficiency was then found for each turbine pressure ratio as well as the net power output and required solar input power at that specific maximum solar-to-mechanical efficiency.

Figs. 5–7 show the maximum solar-to-mechanical efficiency of the complete cycle with the included air-cooled window for four different receiver phase-change temperatures as well as three different off-the-shelf turbochargers as a function of turbine pressure ratio. The maximum solar-to-mechanical efficiency is presented for each turbine pressure ratio, represented by an optimal recuperator geometry.

Figs. 5–7 show that the maximum solar-to-mechanical efficiency increased as the receiver surface temperature increased, especially at higher turbine pressure ratios. Fig. 6 shows that maximum solar-to-mechanical efficiencies in the range of 4%–12% could be achieved (at receiver temperatures of 900 K–1200 K) with the *GT2052* turbocharger's range of pressure ratios.

Tables 2–4 show the maximum data points correlating to Figs. 5–7. For example, the required solar input was 24.8 kW to achieve the maximum solar-to-mechanical efficiency of 8%, according to Table 3, with 1.99 kW of shaft power being produced at a pressure ratio of 1.94 and a receiver temperature of 900 K. Fig. 7 shows that solar-to-mechanical efficiencies of up to 12% could be achieved (at 1200 K)

Table 2
Maximum solar-to-mechanical efficiency for *GT1241* and different surface temperatures.

T_s (K)	$r_{t,opt}$	a (mm)	b (mm)	L_{reg} (m)	n	$\dot{W}_{net}$ (W)	M (kg)	$\dot{Q}^*_{tot}$ (kW)	$\eta_{sol,max,max}$
900	2.063	375	2.25	0.5	45	1262	272	17.4	0.072
1000	2.125	450	1.5	0.5	45	1811	325	20.0	0.091
1100	2.438	300	1.5	0.5	45	2859	217	27.9	0.102
1200	2.188	300	2.25	1.25	30	3064	363	25.6	0.120

Table 3
Maximum solar-to-mechanical efficiency for *GT2052* and different surface temperatures.

T_s (K)	$r_{t,opt}$	a (mm)	b (mm)	L_{reg} (m)	n	$\dot{W}_{net}$ (W)	M (kg)	$\dot{Q}^*_{tot}$ (kW)	$\eta_{sol,max,max}$
900	1.938	450	1.5	0.5	45	1985	325	24.8	0.080
1000	1.938	450	1.5	0.5	45	2703	325	27.8	0.097
1100	1.938	450	1.5	0.5	45	3454	325	31.3	0.110
1200	2.375	450	2.25	0.5	45	6098	326	49.6	0.123

Table 4
Maximum solar-to-mechanical efficiency for *GT2860RS* and different surface temperatures.

T_s (K)	$r_{t,opt}$	a (mm)	b (mm)	L_{reg} (m)	n	$\dot{W}_{net}$ (W)	M (kg)	$\dot{Q}^*_{tot}$ (kW)	$\eta_{sol,max,max}$
900	1.625	450	2.25	0.5	45	1939	326	25.8	0.075
1000	1.875	450	1.5	0.5	45	3656	325	39.3	0.093
1100	1.875	450	1.5	0.5	45	4705	325	43.5	0.108
1200	2.063	450	1.5	0.5	45	6804	325	58.3	0.117

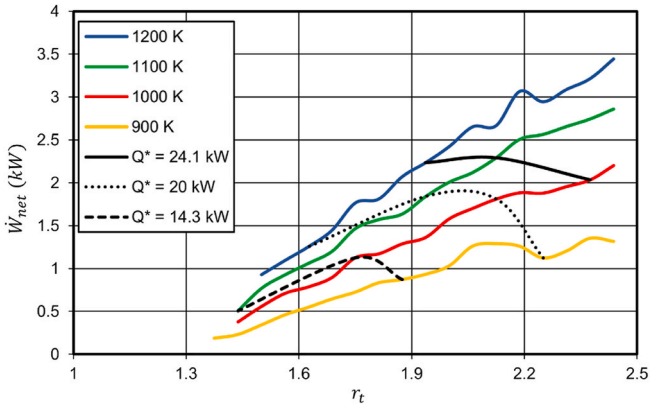

Fig. 8. Net power output at maximum solar-to-mechanical efficiency as a function of turbine pressure ratio, receiver phase-change temperatures (900 K–1200 K) and solar input power (for *GT1241*).

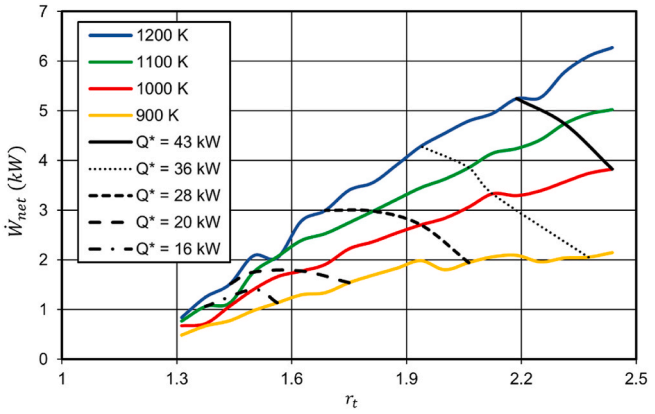

Fig. 9. Net power output at maximum solar-to-mechanical efficiency as a function of turbine pressure ratio, receiver phase-change temperatures (900 K–1200 K) and solar input power (for *GT2052*).

with an off-the-shelf turbocharger (the *GT2860RS*) operating at a turbine pressure ratio of 2.063 and a net power output of 6.8 kW (see Table 4); however, the required solar power was 58.3 kW, which meant that the solar dish and tracking system would have to be very large. For similar solar-to-mechanical efficiencies and receiver phase-change temperatures, a cycle with the *GT1241* turbocharger would require a much smaller solar dish than a cycle with the *GT2052* or *GT2860RS* turbocharger. However, the net power output that could be produced by the *GT1241* turbocharger was lower than for the other two turbochargers. The results show that for nearly all the assumed receiver temperatures, a recuperator with a channel width of 450 mm, channel height of 1.5 mm, length of 0.5 m, and 45 parallel flow channels (90 channels in total) produced maximum solar-to-mechanical efficiency, as shown in Tables 2–4. Only a few recuperators had a slightly larger channel height (2.25 mm).

For each micro-turbine, Figs. 8–10 indicate the cycle's net power output at the maximum solar-to-mechanical efficiency, as a function of the turbine pressure ratio, together with the required solar power at the receiver aperture, $\dot{Q}^*$. The required solar power at the receiver aperture is an indication of the required dish size. Therefore, increased net power output could be produced by the cycle at higher pressure ratios and higher receiver phase-change temperatures. The required solar input power is an indication of the cost of the solar dish because the aperture of the receiver was fixed at 0.25 m × 0.25 m [12]. Figs. 8–10 can thus be viewed as performance maps because they can be used to select specific dish sizes to achieve a certain net power output at a preferred receiver phase-change temperature. As an example, Fig. 9 indicates that, for a solar dish with solar input power of $\dot{Q}^* = 28\,kW$, the expected shaft power output is 2 kW at a receiver phase-change temperature of 900 K and turbine pressure ratio of 2.06, while 3 kW shaft power can be produced at 1200 K at a much lower pressure ratio of 1.69. Fig. 9 also shows that for a receiver at 1000 K, 3.8 kW of net power can be produced at a required solar input of 43 kW and a pressure ratio of 2.44. However, at a lower pressure ratio of 1.94 and a receiver temperature of 1200 K, 4.3 kW of net power can be produced, but at a smaller required solar input of 36 kW. This shows the significance of performance maps for a cost analysis study.

Fig. 11 shows the temperatures at the different positions throughout the cycle (see Fig. 2 for the position numbering) for performance at maximum solar-to-mechanical efficiency when using a *GT2052* off-the-shelf turbocharger with the recuperator geometries mentioned in Table 3. Fig. 11 shows that most of the temperature rise was from State 1 to State 6, which included the compressor, window, recuperator and coiled tube (also see Appendix A for *P-v* and *T-s* diagrams). Fig. 2 indicates that the window was between States 2 and 3, thus considering Fig. 11, the window increased the air temperature on average by about 225 K. The window thus preheated the air before it entered the recuperator and receiver. Furthermore, the exhaust air temperature (at Position 10) was still relatively high, which has the potential for cogeneration.

Fig. 12 shows the pressures at different positions in the cycle for different receiver phase-change temperatures for the *GT2052* micro-turbine operating at the maximum solar-to-mechanical efficiency and optimum pressure ratio (see Table 3). Since the turbochargers considered in this work were sensitive to pressure drop, the small pressure drop in the window (States 2 to 3) and the coiled tube (States 5 to 6) in Fig. 12 was very important to allow for maximum inlet pressure at the turbine (State 7). Fig. 12 shows that the compressor of the *GT2052* turbocharger compressed the air to about 2.1 bar from the ambient pressure of 0.86 bar at a receiver phase-change temperature of 1200 K.

On average, there was a relatively small pressure drop between the window and the coiled tube and this allowed for maximum inlet pressure at the turbine (State 7). The window accounted for between 0.7 kPa and 1.2 kPa of the total pressure drop in the cycle, which was considered acceptable in this study. It must be noted that for some of the receiver phase-change temperatures, the pressure in the cycle was the same as for the other receiver phase-change temperatures and is thus not shown in Fig. 12.

Table 5 shows the *GT2052* turbocharger's shaft speed, compressor and turbine efficiencies, compressor and turbine pressure ratios, and the heat transfer coefficients at different positions in the cycle when the

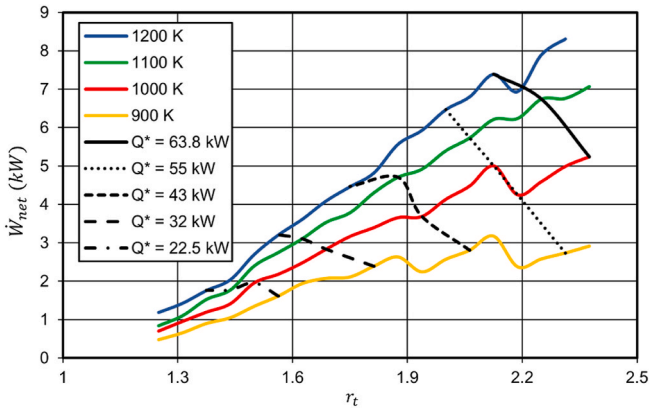

Fig. 10. Net power output at maximum solar-to-mechanical efficiency as a function of turbine pressure ratio, receiver phase-change temperatures (900 K–1200 K), and solar input power (for *GT2860RS*).

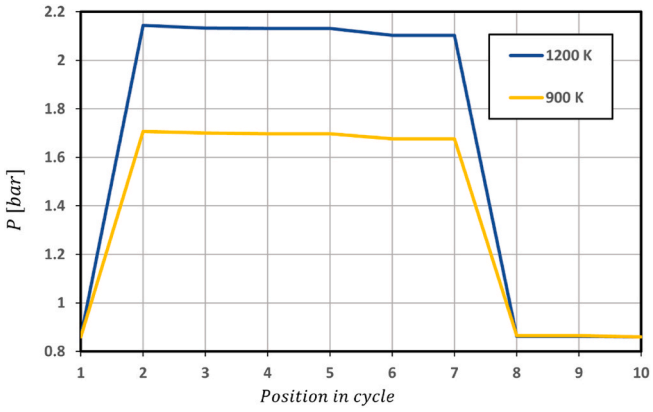

Fig. 12. Pressure in the cycle at different receiver surface temperatures at maximum solar-to-mechanical efficiency (for *GT2052*).

cycle ran at maximum solar-to-mechanical efficiency and the recuperator had the dimensions shown in Table 3. The optimum speed at receiver temperatures of 900 K–1100 K was 135 000 rpm and the optimum turbocharger speed at a receiver temperature of 1200 K was 162 000 rpm. The optimum mass flow rate for each receiver surface temperature at the maximum solar-to-mechanical efficiency was fairly the same at an average of about 0.07 kg/s. The turbine and compressor efficiencies were also relatively constant at an average of about 68% and 72% respectively.

4.2. Effect of the channel width

It was expected that the channel width of the air-cooled window should have a significant impact on the heat transfer rate between the window and the air due to a change in the velocity, Reynolds number and heat transfer coefficient. A parametric analysis was conducted with the *GT2052* micro-turbine at a fixed pressure ratio of 1.938 and recuperator dimensions of $a = 450$ mm, $b = 1.5$ mm, $L_{reg} = 0.5$ m and $n = 45$ channels (90 channels in total). This allowed for easier comparison between the different receiver surface temperatures. The channel width was thus treated as a parameter; and the air-cooled window's pressure drop (from Positions 2 to 3 in Fig. 2), temperature change and glass surface temperature were compared. The channel width mentioned in the results refers to the distance between two glass panes where the HTF passes in between. It was expected that as the channel width was increased, the pressure drop across the channel would decrease and the cooling effectiveness of the HTF would also decrease. Figs. 13–18 show the results of the parametric analysis, which include the pressure drop and temperature change across the cooling channel as well as the solar-to-mechanical efficiency and glass surface temperature.

Table 5
Performance at maximum solar-to-mechanical efficiency for *GT2052* at different surface temperatures.

	900 K	1000 K	1100 K	1200 K
N' (rpm)	135 000	135 000	135 000	162 000
$\dot{m}$ (kg/s)	0.0771	0.0731	0.0696	0.0878
η_t	0.692	0.681	0.669	0.671
η_c	0.736	0.729	0.723	0.704
r_c	1.992	1.9918	1.9926	2.4932
r_t	1.9375	1.9375	1.9375	2.4375
h_{rec} (W/m^{2}K)	55.5	54.7	53.9	65.6
$h_{reg.hot}$ (W/m^{2}K)	135.8	145.7	155.4	109.8
$h_{reg.cold}$ (W/m^{2}K)	134.1	144.0	154.0	107.9
$h_{win.chn.avg}$ (W/m^{2}K)	49.88	49.22	46.17	58.26

Fig. 13 shows that the pressure drop decreased as the channel width increased, whereas Fig. 14 indicates that the temperature change of the air as it flowed through the cooling channel decreased as the channel width increased. Thus, a smaller channel width would cool the glass panes better than a larger channel width; however, a smaller channel width would lead to an increased pressure drop across the air-cooled window, which could be detrimental to the micro-turbines considered in this cycle. A trade-off would have to be made between cooling the glass effectively and having a low enough pressure drop to ensure maximum inlet pressure at the turbine.

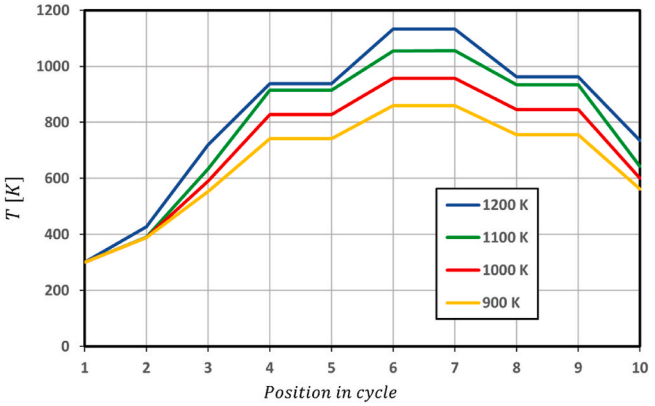

Fig. 11. Temperature in the cycle at different receiver surface temperatures at maximum solar-to-mechanical efficiency (for *GT2052*).

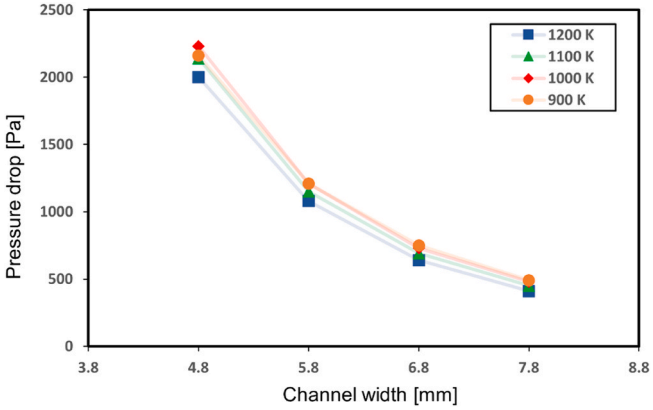

Fig. 13. Pressure drop across the cooling window for different cooling channel widths and receiver surface temperatures (for *GT2052*).

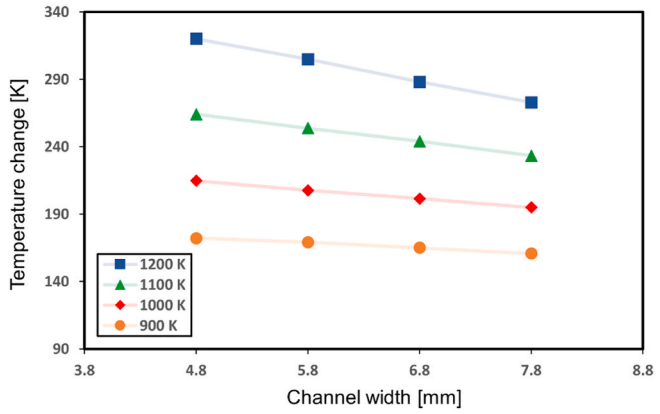

Fig. 14. Temperature change of the HTF across the cooling window for different cooling channel widths and receiver surface temperatures (for *GT2052*).

Figs. 15 and 16 show the solar-to-mechanical efficiency and net power output as a function of the channel width. The solar-to-mechanical efficiency increased on average by about 1.3% and the net power output by about 0.24 kW as the channel width varied from 4.8 mm to 7.8 mm. A larger channel width would thus be favourable when a large solar-to-mechanical efficiency and net power output were desired. Figs. 15 and 16 also indicate that for a channel width of above 5.8 mm, the change in the solar-to-mechanical efficiency and net power output between the different channel widths was small.

Figs. 17 and 18 show the average glass surface temperatures for each division on one of the four sides for a receiver temperature of 900 K and 1200 K. The top glass temperature is not included for display purposes. Only one of the four sides is shown because all four sides would have the same temperature due to the 0° dish tracking error assumption that was made. The glass surface temperature shown in Figs. 17 and 18 is an average over the two glass panes that form the cooling channel. A smaller channel width shows a lower average surface temperature per glass division and a lower receiver tube temperature also shows a lower average glass surface temperature. This was expected since the smaller channel width increased the velocity of the air and thus the Reynolds number of the flow. An increased Reynolds number led to an increased heat transfer coefficient on the inside of the cooling channel. As an example, if quartz glass were used for this application, with an average working temperature of about 1100 K, a channel width of 7.8 mm and a receiver phase-change temperature of 1200 K would produce a maximum glass surface temperature of 1115 K (see Fig. 18).

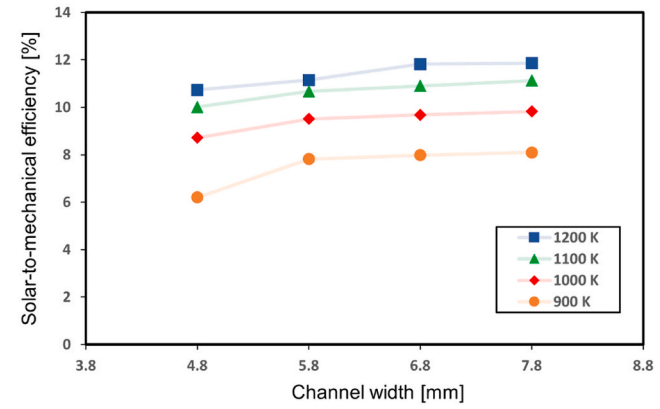

Fig. 15. Solar-to-mechanical efficiency for different cooling channel widths and receiver surface temperatures (for *GT2052*).

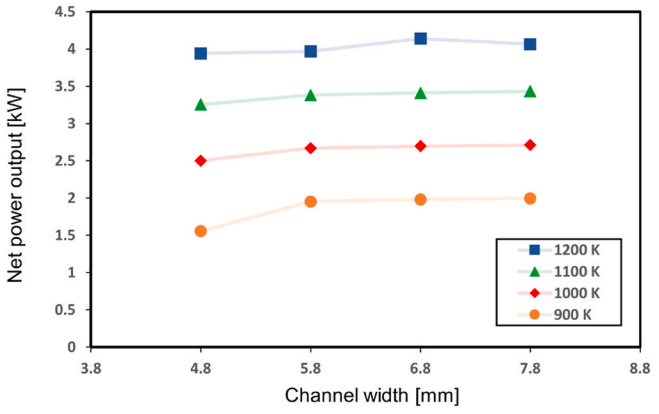

Fig. 16. Net power output for different cooling channel widths and receiver surface temperatures (for *GT2052*).

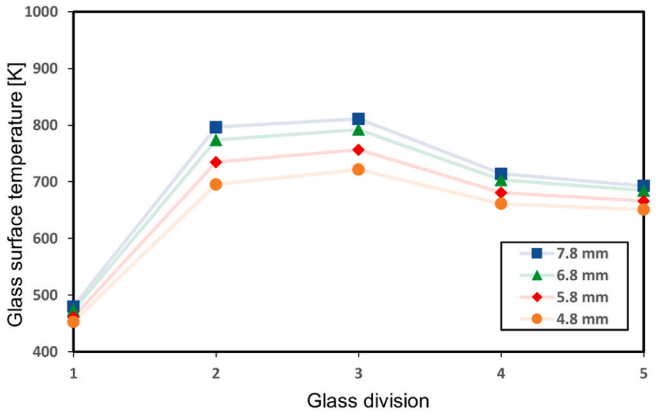

Fig. 17. Glass surface temperature as a function of channel width for receiver surface temperature of 900 K (for *GT2052*).

A trade-off would have to be made between pressure drop and cooling effectiveness. Considering the above results, a channel width of 5.8 mm would produce a pressure drop of between 1 kPa and 1.2 kPa (see Fig. 13) and a temperature change of the HTF over the window of between 170 K and 305 K for the different receiver surface temperatures.

4.3. Performance impact of window

Tables 6–8 summarise the optimum cycle properties and recuperator

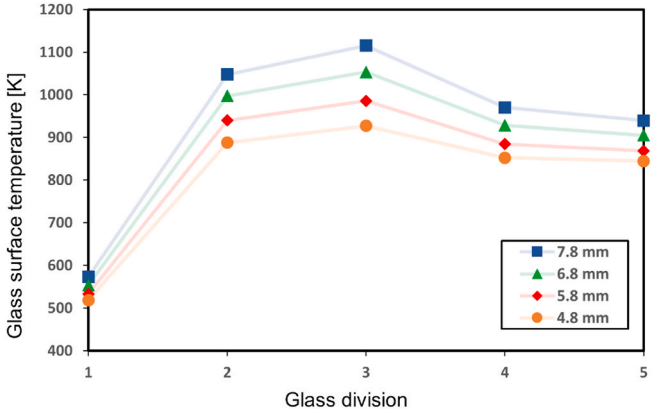

Fig. 18. Glass surface temperature as a function of channel width for receiver surface temperature of 1200 K (for *GT2052*).

Table 6
Comparison of cycle properties with and without a cooling window for the *GT1241* turbo.

Turbo	T_s (K)		$r_{t,opt}$	a (mm)	b (mm)	L_{reg} (m)	n	M (kg)	$\eta_{sol,max}$	$\dot{Q}^*_{tot}$ (kW)	$\dot{Q}_w$ (kW)	$\dot{W}_{net}$ (kW)	*EUF*
GT1241	900	Without window	2.063	450	1.5	0.5	45	325	0.127	9.0	3.5	1.1	51%
		With window	2.063	375	2.3	0.5	45	272	0.072	17.4	8.8	1.3	58%
	1000	Without window	2.188	450	1.5	0.5	45	325	0.158	11.5	3.9	1.8	50%
		With window	2.125	450	1.5	0.5	45	325	0.091	20.0	9.6	1.8	57%
	1100	Without window	2.188	450	1.5	0.5	45	325	0.175	13.3	3.8	2.3	46%
		With window	2.438	300	1.5	0.5	45	217	0.102	27.9	13.5	2.9	58%
	1200	Without window	2.438	450	1.5	0.5	45	325	0.182	17.8	4.9	3.3	46%
		With window	2.188	300	2.3	1.3	30	363	0.120	25.6	10.2	3.1	52%

Table 7
Comparison of cycle properties with and without a cooling window for the *GT2052* turbo.

Turbo	T_s (K)		$r_{t,opt}$	a (mm)	b (mm)	L_{reg} (m)	n	M (kg)	$\eta_{sol,max}$	$\dot{Q}^*_{tot}$ (kW)	$\dot{Q}_w$ (kW)	$\dot{W}_{net}$ (kW)	*EUF*
GT2052	900	Without window	1.938	450	1.5	0.5	45	325	0.152	13.0	5.5	2.0	58%
		With window	1.938	450	1.5	0.5	45	325	0.080	24.8	13.3	2.0	62%
	1000	Without window	1.938	450	1.5	0.5	45	325	0.182	14.6	5.4	2.7	55%
		With window	1.938	450	1.5	0.5	45	325	0.097	27.8	14.5	2.7	62%
	1100	Without window	1.938	450	1.5	0.5	45	325	0.201	16.6	5.3	3.3	52%
		With window	1.938	450	1.5	0.5	45	325	0.110	31.3	15.8	3.5	61%
	1200	Without window	2.375	450	1.5	0.5	45	325	0.220	26.5	8.9	5.8	56%
		With window	2.375	450	2.3	0.5	45	326	0.123	49.6	25.2	6.1	63%

dimensions with and without the proposed cooling window for each of the three different turbochargers. To compare the results of this study with the results of previous work by Le Roux and Sciacovelli [12], in which the cycle had no window, the window code was added to the original code of Le Roux and Sciacovelli [12]. The results of Le Roux and Sciacovelli [12] could therefore be directly reproduced (see Appendix B for further validation of the code). The only other modifications to the code were the recuperator length, which was allowed to range from 0.5 m to 3.5 m (instead of from 1.5 m to 4.5 m), as indicated in Table 1, and a lower tolerance of 0.01 for the iterations (higher resolution) was used.

The *EUF* was calculated as described in Section 3.3.4 with $\dot{Q}_w = \eta \dot{Q}_{max,T_{11-1}}$. Each row compares the results of the cycle without the window with the results of the cycle with the window for each turbocharger and receiver phase-change temperature. It should be noted that the properties given in Tables 6–8 are for the optimum performance of the cycle (for maximum solar conversion efficiency). Compared with the optimal recuperators in the cycles without the window, the optimal recuperators in the current study had the same dimensions for most of the results presented. The exceptions were at a receiver phase-change temperature of 900 K or 1200 K for all three turbochargers, where the recuperator channel height was about 0.8 mm larger than for the cycle without the window. Tables 6–8 shows that the optimum turbine pressure ratios were slightly different from those of the cycles without the cooling window, except for the *GT2052* turbocharger, which had the same optimum turbine pressure ratios.

For each of the turbochargers, a higher solar input power was required to reach maximum solar conversion efficiency compared to the cycle without the window. Results also show that the maximum solar-to-mechanical efficiency was on average between 41% and 45% lower than for the cycle without a window. However, the *EUF* was on average 9%–11% higher than for the cycle without the cooling window. Note that a higher cycle exhaust temperature would lead to a higher *EUF* according to Eq. (31). The cycle exhaust temperature was on average 46%, 50% and 43% higher (with temperature in Kelvin) for the *GT1241*, *GT2052* and *GT2860RS* turbochargers respectively. A higher *EUF* means that the cycle converted the available solar power more efficiently into useable power and heat. The window also essentially acted as a heat exchanger that preheated the air before it went into the recuperator.

5. Discussion

This research considered three off-the-shelf turbochargers and different recuperator dimensions to determine the impact of a novel cooling window on the performance of a recuperated solar-dish Brayton cycle with a fixed solar receiver geometry operating at different PCM temperatures. The receiver considered in this study differed from those available in the literature because a novel cooling window, using air directly from the compressor, was implemented on the inside of the receiver to reduce heat losses from the receiver to the environment. The results of the cycle utilising this receiver and novel cooling window were compared with the results of a previous study by Le Roux and Sciacovelli [12], which did not include the cooling window.

For the cycle with a cooling window, the turbocharger that would produce the highest solar-to-mechanical efficiency while still having an acceptable required solar input was found to be the *GT2052*. The *GT2052* turbocharger allowed for the best performance at a turbine pressure ratio of 1.94 and a mass flow rate of 0.07 kg/s, with the recuperator dimensions being as follows: a channel width of 450 mm, channel height of 1.5 mm, channel length of 0.5 m, and 45 parallel flow channels (90 channels in total). A receiver phase-change temperature of 1100 K or below would achieve the maximum solar-to-mechanical efficiency while having an acceptable required solar input power (and thus dish size) and keeping the glass window cool enough for it to not shatter. It was also found that the cooling channel width had to be between 5 mm and 5.8 mm to keep the glass cool enough while maintaining an acceptable pressure drop across the cooling window. However, this conceptual study showed that it might not be feasible to implement the cooling window, except where a higher cycle exhaust temperature is preferred for cogeneration.

It should be noted that the results of this study are limited to open and recuperated solar-dish Brayton cycles implementing an off-the-shelf

Table 8
Comparison of cycle properties with and without a cooling window for the *GT2860RS* turbo.

Turbo	T_s (K)		$r_{t,opt}$	a (mm)	b (mm)	L_{reg} (m)	n	$M(kg)$	$\eta_{sol,max}$	$\dot{Q}^{*}_{tot}$ (kW)	$\dot{Q}_w$ (kW)	$\dot{W}_{net}$ (kW)	EUF
GT2860RS	900	Without window	1.625	450	1.5	0.5	45	325	0.149	12.8	5.5	1.9	57%
		With window	1.625	450	2.3	0.5	45	326	0.075	25.8	14.1	1.9	62%
	1000	Without window	2.125	450	1.5	0.5	45	325	0.176	27.9	12.6	4.9	63%
		With window	1.875	450	1.5	0.5	45	325	0.093	39.3	21.2	3.7	63%
	1100	Without window	1.875	450	1.5	0.5	45	325	0.198	23.2	8.8	4.6	58%
		With window	1.875	450	1.5	0.5	45	325	0.108	43.5	22.8	4.7	63%
	1200	Without window	2.125	450	1.5	0.5	45	325	0.215	33.5	12.6	7.2	59%
		With window	2.063	450	1.5	0.5	45	325	0.117	58.3	30.2	6.8	63%

Garrett turbocharger as a micro-turbine, using a parabolic solar dish (with a rim angle of 45°) to concentrate the solar irradiation onto an integrated open-cavity coiled-tube rectangular receiver with PCM thermal storage.

6. Conclusion and future work

6.1. Conclusion

The following points list the important findings from this work:

- The required solar input power and the cycle's exhaust temperature were higher than the cycle without the window.
- The maximum solar-to-mechanical efficiencies of the cycle with the novel cooling window were, on average, between 41% and 45% lower than for the cycle without a cooling window.
- The higher exhaust temperature of the cycle with the window led to a higher *EUF* than for the cycle without the window.
- The *EUF* was on average 9%–11% higher, and therefore, the cycle with the window had more potential for cogeneration, such as water heating or thermal energy storage.
- The *GT2052* turbocharger would produce the highest solar-to-mechanical efficiency in a cycle with a cooling window and a recuperator, while still having acceptable solar input power requirements.
- The cooling channel width had to be between 5 mm and 5.8 mm to keep the glass at a temperature of 1100 K or lower while maintaining an acceptable pressure drop across the cooling window.

6.2. Future work

This research served as an initial conceptual study from which further work could be done. There are a few possibilities regarding future work. The study only investigated the cooling channel width as a parameter and future work could include the cooling channel width as a variable in the study. The recuperator variables in this study were limited to a specific range (for the sake of comparison with previous work) and future work could include a larger range of variables to ensure a broader analysis of the cycle with the novel cooling window. More realistic pressure drop and heat loss values can be implemented for the connecting pipes (including the recuperator inlets and outlets), since the current model assumed these losses to be negligible. A non-linear routine such as Newton's method could be used to increase the accuracy of the glass surface temperature and net heat transfer rate calculations. Increased resolution on each glass channel using CFD and the modelling of the two sides of the glass channel separately is also recommended, however, at a much higher computational cost. Future work could also include experimentally testing the air-cooled window concept and comparing it with the results of this study. Lastly, it is recommended that a cost analysis and optimisation be done to further compare the two cycles (with and without the cooling window). However, this initial and conceptual study showed that it might not be feasible to implement the novel cooling window, except where a higher *EUF* is preferred when including cogeneration.

CRediT authorship contribution statement

J.H. de Beer: Data curation, Formal analysis, Investigation, Methodology, Software, Validation, Visualization, Writing – original draft, Writing – review & editing. **W.G. le Roux:** Conceptualization, Funding acquisition, Methodology, Project administration, Resources, Software, Supervision, Validation, Writing – original draft, Writing – review & editing. **A. Sciacovelli:** Conceptualization, Funding acquisition, Writing – review & editing. **J.P. Meyer:** Funding acquisition, Resources, Supervision, Writing – review & editing.

Declaration of competing interest

The authors declare that they have no known competing financial interests or personal relationships that could have appeared to influence the work reported in this paper.

Acknowledgements

The authors would like to acknowledge the support of the Department of Science and Innovation (DSI) of South Africa as well as the Royal Society of the United Kingdom (Newton Mobility Grant: NMG\R2 \170082).

Appendix A. *P-v* and *T-s* diagrams

Fig. A-1 shows the pressure-specific volume diagram and Fig. A-2 the temperature-entropy diagram for the *GT2052* turbocharger at 900 K, at the optimum pressure ratio and with recuperator geometries as shown in Table 3. The numbers on the diagrams correspond to the numbering system in Fig. 2 and can be compared with Figs. 11 and 12. Fig. A-1 shows the pressure drop in the cooling window, recuperator, receiver and turbine. Fig. A-2 shows the entropy generation in the compressor and turbine. Note that $T_{10} > T_3$ and $T_9 > T_4$, and that the recuperator hot-side effectiveness was 96.1% and the cold-side effectiveness was 92.7%. However, the recuperator pressure drop was relatively small, showing how the theoretically optimised recuperator benefitted the cycle's performance.

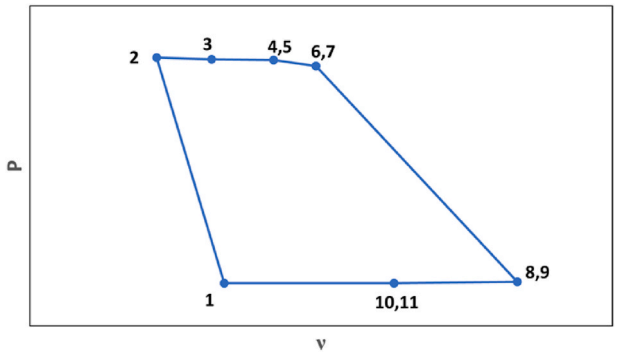

Fig. A-1. Pressure-specific volume diagram for the GT2052 turbocharger at 900 K, optimum pressure ratio and optimum recuperator geometries.

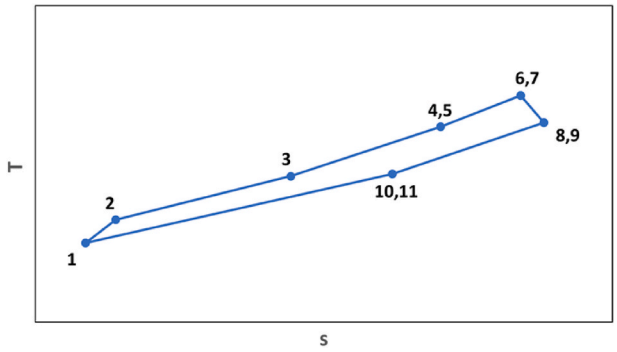

Fig. A-2. Temperature-entropy diagram for the *GT2052* turbocharger at 900 K, optimum pressure ratio and optimum recuperator geometries.

Appendix B. Model verification

The numerical method was verified by considering the difference between the calculation of the net power output with an exergy analysis, the first law of thermodynamics and a heat balance. Eq. (B-1) shows the net power output calculation for the shaft using the first law of thermodynamics (see Fig. 2). Eq. (B-2) shows the net power output calculation using a heat balance on the control volume of the cycle shown in Fig. 2. Thus, the results found using Eq. (28) which were derived using an exergy analysis can be compared to the results found using Eq. (B-1) and Eq. (B-2). D_1 in Eq. (B-3) and D_2 in Eq. (B-4) represent the difference between the calculations of $\dot{W}_{net}$.

$$X_1 = \dot{m}c_{p,0}(T_7 - T_8) - \dot{m}c_{p,0}(T_2 - T_1) \tag{B-1}$$

$$X_2 = \dot{Q}^{*}_{tot} - \dot{m}c_{p,0}(T_{10} - T_1) - \left(\dot{Q}_{loss,win} + \dot{Q}_{loss,cond,rec} + \dot{Q}_{loss,reg}\right) \tag{B-2}$$

$$D_1 = \left((\dot{W}_{net} - X_1)/X_1\right) \times 100 \tag{B-3}$$

$$D_2 = \left((\dot{W}_{net} - X_2)/X_2\right) \times 100 \tag{B-4}$$

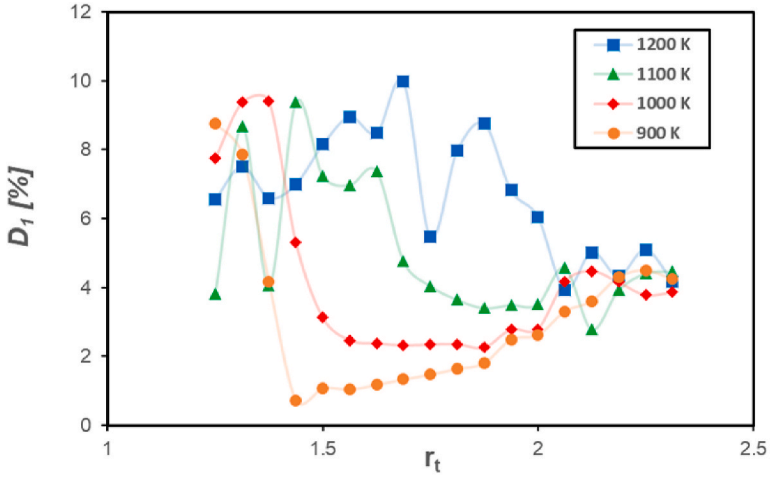

Fig. B-1. D_1 as a function of pressure ratio for the *GT2052* turbocharger at maximum solar-to-mechanical efficiency.

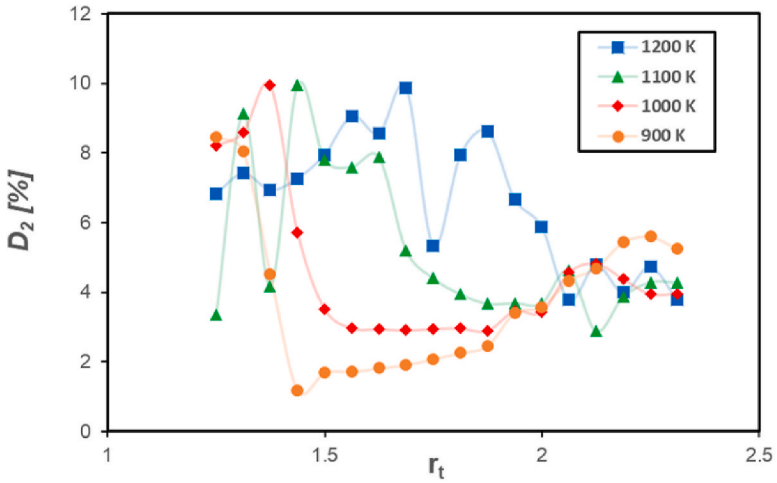

Fig. B-2. D_2 as a function of pressure ratio for the *GT2052* turbocharger at maximum solar-to-mechanical efficiency.

Figs. B-1 and B-2 show D_1 and D_2 as a function of the pressure ratio for the *GT2052* turbocharger. Table B-1 shows D_1 and D_2 for different receiver temperatures and turbochargers corresponding to the geometries given in Table 2 to Table 4. The differences are attributed to iteration tolerances (which were chosen to limit computational time), as well as the use of constant-pressure specific heat values that were used throughout the simulations (as was done in the original code [12]), instead of using enthalpy values. The constant pressure specific heat values were calculated at the average temperatures between nodes. A difference of up to 10% (for both D_1 and D_2) was therefore considered to be acceptable.

Table B-1
D_1 and D_2 for different receiver temperatures and turbochargers at optimal performance

T_s [K]	GT1241		GT2052		GT2860RS	
	D_1 [%]	D_2 [%]	D_1 [%]	D_2 [%]	D_1 [%]	D_2 [%]
900	9.1	9.8	1.8	2.5	1.1	1.7
1000	4.3	4.9	2.3	2.9	2.2	2.9
1100	9.7	9.7	3.4	3.7	2.6	3.0
1200	5.4	5.6	4.2	3.8	2.5	2.4

References

[1] A. Pietsch, D.J. Brandes, Advanced solar Brayton space power systems, in: Proceedings of the 24th Intersociety Energy Conversion Engineering Conference, 6–11 Aug. 1989, 1989, pp. 911–916.
[2] A. Giostri, M. Binotti, C. Sterpos, G. Lozza, Small scale solar tower coupled with micro gas turbine, Renew. Energy 147 (1) (2020) 570–583.
[3] X.L. Li, X.L. Xia, Z.H. Li, X. Chen, Effects of double windows on optical and thermal performance of solar receivers under concentrated irradiation, Sol. Energy 184 (2019) 331–344.
[4] A. Kasaeian, A. Kouravand, M.A.V. Rad, S. Maniee, F. Pourfayaz, Cavity receivers in solar dish collectors: a geometric overview, Renew. Energy 169 (2021) 53–79.
[5] J. Coventry, C. Andraka, Dish systems for CSP, Sol. Energy 152 (2017) 140–170.
[6] K. Wang, H. Wu, D. Wang, Y. Wang, Z. Tong, F. Lin, A.G. Olabi, Experimental study on a coiled tube solar receiver under variable solar radiation condition, Sol. Energy 122 (2015) 1080–1090.
[7] M.A. Bashir, A. Giovannelli, H.M. Ali, Design of high-temperature solar receiver integrated with short-term thermal storage for dish-micro gas turbine systems, Sol. Energy 190 (2019) 156–166.
[8] M. Liu, W. Saman, F. Bruno, Review on storage materials and thermal performance enhancement techniques for high temperature phase change thermal storage systems, Renew. Sustain. Energy Rev. 16 (2012) 2118–2132.
[9] A. Giovannelli, M.A. Bashir, E.M. Archilei, High-temperature solar receiver integrated with a short-term storage system, AIP Conf. Proc. 1850 (2017), 050001, https://doi.org/10.1063/1.4984405.
[10] W.G. Le Roux, T. Bello-Ochende, J.P. Meyer, The efficiency of an open-cavity tubular solar receiver for a small-scale solar thermal Brayton cycle, Energy Convers. Manag. 84 (2014) 457–470.
[11] W.G. Le Roux, T. Bello-Ochende, J.P. Meyer, Optimisation of an open rectangular cavity receiver and recuperator used in a small-scale solar thermal Brayton cycle with thermal losses, in: 10th International Conference on Heat Transfer, Fluid Mechanics and Thermodynamics, 2014, pp. 499–507. Orlando, Florida.
[12] W.G. Le Roux, A. Sciacovelli, Recuperated solar-dish Brayton cycle using turbocharger and short-term thermal storage, Sol. Energy 194 (2019) 569–580.
[13] K.J. Craig, M. Slootweg, W.G. Le Roux, T.M. Wolff, J.P. Meyer, Using CFD and ray tracing to estimate the heat losses of a tubular cavity dish receiver for different inclination angles, Sol. Energy 211 (2020) 1137–1158.
[14] F. Cui, Y. He, Z. Cheng, Y. Li, Study on combined heat loss of a dish receiver with quartz glass cover, Appl. Energy 112 (2013) 690–696.
[15] S. Fischer, E. Hahne, The Effect of Different Glass Covers on the Yearly Energy Gain of a Solar Collector, University of Stuttgart, Stuttgart, Germany, 2000.
[16] W. Fuqiang, T. Jianyu, M. Lanxin, W. Chengchao, Effects of glass cover on heat flux distribution for tube receiver with parabolic trough collector system, Energy Convers. Manag. 90 (2014) 47–52.
[17] I. Subedi, T.J. Silverman, M.G. Deceglie, N.J. Podraza, Emissivity of solar cell cover glass calculated from infrared reflectance measurements, Sol. Energy Mater. Sol. Cell. 190 (2019) 98–102.
[18] R. Uhlig, M. Röger, Development of a Window Cooling for High-Temperature Solar Receivers. 22nd CAD-FEM Users' Meeting 2004, International Congress on FEM Technology, Germany, 2004.
[19] P. Wang, J.B. Li, F.W. Bai, D.Y. Liu, C. Xu, L. Zhao, Z.F. Wang, Experimental and theoretical evaluation on the thermal performance of a windowed volumetric solar receiver, Energy 117 (2016) 652–661.
[20] Y.C.S. Too, M.D. López, H. Cassard, G. Duffy, R. Benito, R. Navio, Thermal performance and operation of a solar tubular receiver with CO2 as the heat transfer fluid, J. Sol. Energy Eng. 139 (2017), 041004-2 - 041004-9.
[21] P.D. Malali, S.K. Chaturvedi, T. Abdel-Salam, Performance optimization of a regenerative Brayton heat engine coupled with a parabolic dish solar collector, Energy Convers. Manag. (2017) 85–95.
[22] R.K. Shah, Compact heat exchangers for microturbines, in: Proceedings of the Fifth International Conference on Enhanced, Compact and Ultra-compact Heat Exchangers, Science, Engineering and Technology, Hoboken, USA, 2005 (CHE2005 – 31).
[23] J.C. Ho, K.J. Chua, S.K. Chou, Performance study of a microturbine system for cogeneration application, Renew. Energy 29 (7) (2004) 1121–1133.

[24] T. Wendelin, A. Dobos, A. Lewandowski, SolTrace: a Ray-Tracing Code for Complex Solar Optical Systems, National Renewable Energy Laboratory, 2013.
[25] Y.A. Çengel, A.J. Ghajar, Heat and Mass Transfer: Fundamentals and Applications, fifth ed., McGraw Hill Education, New York, 2015.
[26] V. Gnielinski, New equations for heat and mass transfer in turbulent pipe and channel flow, Int. Chem. Eng. 16 (1976) 359–368.
[27] B.S. Petukhov, Heat Transfer and Friction in Turbulent Pipe Flow with Variable Physical Properties. Advances in Heat Transfer, vol. 6, Academic Press, New York, 1970.
[28] S. Paitoonsurikarn, K. Lovegrove, A new correlation for predicting the free convection loss from solar dish concentrating receivers, in: Proceedings of 44th ANZSES Conference, 2006, 13-15 September, Canberra, Australia.
[29] S. Paitoonsurikarn, K. Lovegrove, On the study of convection loss from open cavity receivers in solar paraboloidal dish applications, in: Proceedings of the 40th ANZSES Conference, 2003, 26-29 November, Melbourne, Australia.
[30] S. Paitoonsurikarn, T. Taumofeloau, K. Lovegrove, Estimation of convection loss from paraboloidal dish cavity receivers, in: Proceedings of the 42nd ANZSES Conference vol. 28, 2004. November - 1 December, Perth, Australia.
[31] R. Pendyala, Y.S. Wong, S.U. Ilyas, CDF simulations of natural convection heat transfer in enclosures with varying aspect ratios, Chem. Eng. Trans. 45 (2015) 793–799.
[32] W.G. Le Roux, Thermodynamic Optimisation and Experimental Collector of a Dish-Mounted Small-Scale Solar Thermal Brayton Cycle, University of Pretoria, Thesis, 2015.
[33] W.G. Le Roux, Feasibility study of a hybrid small-scale dish-mounted solar thermal Brayton cycle with cogeneration, in: Proceedings of the 16th International Heat Transfer Conference (IHTC16-24185), 2018, pp. 7929–7936. Beijing, China.